An Extensive Analysis of Low-Level IR Transmission Measurements taken over a 15 km Path during EOPACE with IRBLEM

J. Luc Forand[a], Denis Dion[a], Mike Duffy[a], Stuart Gathman[b], Kathleen Littfin[b], Arie de Jong[c], Gerrit de Leeuw[c], and K. Davidson[d]

[a]Defence Research Establishment Valcartier
2459 Pie XI Blvd. N., Val-Belair, QC, Canada G3J 1X5
[b]Space and Naval Warfare Systems Center, Propagation Division
49170 Propagation Path, San Diego, CA, USA 92152-7385
[c]TNO Physics and Electronics Laboratory
P.O. Box 96864, 2509 JG The Hague, The Netherlands
[d]Naval Postgraduate School (NPS), Code 63/DS
589 Dyer Road, Room 252, Monterey, CA, USA 93493-5000

ABSTRACT

Results of over 300 far IR and mid IR transmission measurements taken during several EOPACE (EO Propagation Assessment in Coastal Environments) intensive operational periods (IOP's) over the low-level 15 km transmission path across San Diego bay are presented. A thorough comparison with calculations obtained using simultaneously measured bulk meteorological parameters with the IR Boundary Layer Model (IRBLEM), illustrate the effects that refractance, aerosol extinction and molecular extinction can have on the transmission. Discrepancies between the transmission measurements and the model's predictions are identified and investigated by varying various model parameters, and looking at available measured aerosol size distributions and refraction measurements over the path. Comparison with the measured transmissions are reasonably good and show that the total transmission depends critically on all three effects, with the molecular transmittance depending upon the water vapour density and the characteristics of the IR source and detector, the aerosol transmittance upon the visibility (aerosol concentration), and the refractive effects on the stability of the marine boundary layer or the virtual potential air-sea temperature difference.

Keywords: refraction, transmission, marine boundary layer, aerosol extinction, infrared, IRBLEM, EOPACE

1. INTRODUCTION

The two intensive operational periods (IOPs) of the EO Propagation Assessment in Coastal Environments (EOPACE) campaign, that were conducted in San Diego during March and April 1996 and November 1996, were good opportunities to obtain excellent transmission data within the marine boundary layer (MBL) and to compare them to predictions made by the IR Boundary Layer Effects Model (IRBLEM). This was made possible due to the transmission data obtained by Arie de Jong of TNO over the 15 km transmission path, the basic meteorological data obtained at both ends and in the middle of the transmission path, and the aerosol size distribution measurements taken over the path by Stewart Gathman of SPAWAR.

To better understand how the data was obtained and how the analysis was performed using IRBLEM[1], the following section presents a brief discussion of the effects which can affect the transmission of IR radiation in the MBL, and the modules that IRBLEM uses to model them. The following section gives a short description of the various meteorological and transmission equipment that was used and their locations around San Diego Bay. The last three sections present the results of the study, and some conclusions.

Further author information -
Email: Luc.Forand@drev.dnd.ca; WWW:http://www.drev.dnd.ca; Tel.:(418)-844-4503; Fax: (418)-844-4511

Part of the SPIE Conference on Propagation and Imaging through the Atmosphere II • San Diego, California • July 1998
SPIE Vol. 3433 • 0277-786X/98/$10.00

2. IR TRANSMISSION IN THE MARINE BOUNDARY LAYER

The marine boundary layer (MBL) is a region of the atmosphere which extends from the marine surface to a height which may vary from 20 to several 100 meters. As the air and marine surface can often be at different temperatures, this region of the atmosphere, through convection and air transport, can possess strong vertical gradients in temperature, water vapour density, and aerosol concentration. The MBL is also a region that is a source of maritime aerosols and a sink, particularly in coastal regions, for terrestrial aerosols (particulates). The various gradients, the concentrations, type and particle distribution of the aerosols, and the amount of water vapour in the MBL all have important consequences on the transmission of IR radiation. Temperature gradients can cause significant refractive effects (mirage formation, focussing and defocussing), while the composition of the MBL determines the amount of IR radiation that is scattered or absorbed.

Following Refs. 2 & 3, for a spherical wavefront of frequency, ν, the intensity, $I(\mathbf{r},\nu)$, at some vector position, $\mathbf{r}$, from a point source can be expressed by:

$$I(\mathbf{r},\nu) = \frac{I_0(\nu)}{r^2}\sum_{j=1}^{m}\rho_j(\mathbf{r},\nu)\tau_{jM}(\mathbf{r},\nu)\tau_{jA}(\mathbf{r},\nu) = \frac{I_0(\nu)}{r^2}\sum_{j=1}^{m}T_j(\mathbf{r},\nu) = \frac{I_0(\nu)}{r^2}T(\mathbf{r},\nu), \quad (1)$$

where m is the number of images (m is greater than 1 when there are secondary images or mirages), j is an image index,

$$T(\mathbf{r},\nu) = \sum_{j=1}^{m}T_j(\mathbf{r},\nu) = \sum_{j=1}^{m}\rho_j(\mathbf{r},\nu)\tau_{jM}(\mathbf{r},\nu)\tau_{jA}(\mathbf{r},\nu) \quad (2)$$

is the total transmission, and

$$\tau_{jx}(\mathbf{r},\nu) = e^{-\int_0^r \alpha_x(r(s_j),\nu)\,ds_j} \quad ; \textit{for } x = M, A \quad (3)$$

is either the molecular transmittance, $\tau_{jM}(\mathbf{r},\nu)$, or the aerosol transmittance, $\tau_{jA}(\mathbf{r},\nu)$, $\alpha_x(\mathbf{r},\nu)$ is the respective extinction coefficient, and the integral is taken over the path followed by the ray creating the image. $I_0(\nu)$ is the total emitted intensity, and $\rho(\mathbf{r},\nu)$ is the refractance at the vector position, $\mathbf{r}$ for frequency, ν. For straight rays (i.e., no refraction) the refractance equals 1; however, if the rays are focussed, the refractance becomes greater than 1, and if they are defocussed, the refractance becomes less than 1. Thus, the refractance can be thought of as an optical amplifier with gain ρ.

The IR Boundary Layer Effects Model (IRBLEM ver. 2.7.1)[1] has been designed to calculate each of the above terms for rays which propagate within the MBL. Figure 1 shows IRBLEM's internal modular structure with the meteorological inputs situated at the top and the various outputs at the bottom. The required meteorological data is passed to each of the four subsequent routines which calculate the molecular extinction ($\tau_M(\nu)$), the vertical refractivity profile ($N(h)$), the vertical refractivity structure parameter profile ($C_n^2(h)$; turbulence), and the vertical aerosol extinction profile ($\alpha_A(h)$). The molecular extinction is spectrally calculated using MODTRAN[4] in the horizon mode for the height at which the air temperature was measured, the desired

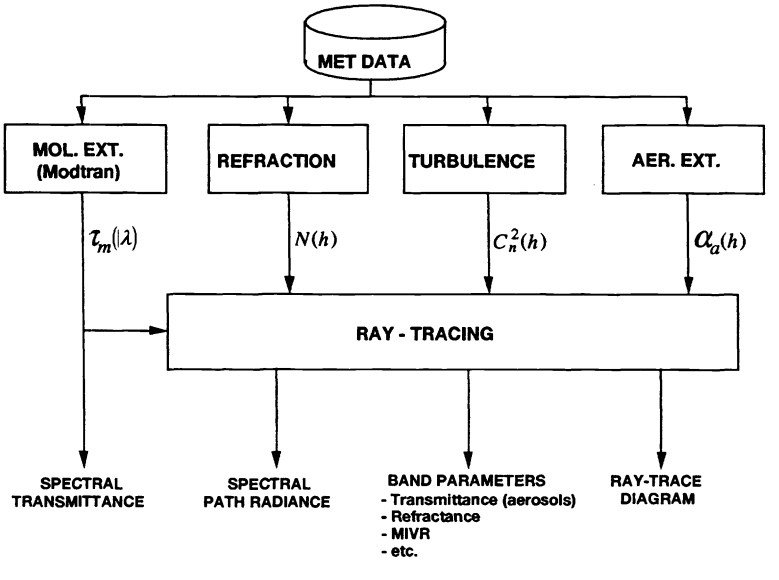

Figure 1 - Schematic diagram showing the modular structure of IRBLEM.

wavelength band, and for a nominal resolution of 5 cm^{-1}. Thus, the molecular extinction is independent of any vertical gradients. The vertical structure parameter profile is not used in this study and will not be discussed any further. For the calculation of the vertical aerosol extinction coefficient profile, a module was provided by TNO[1], that allows the user to select one of three models to estimate the aerosol extinction at 10 meters above the surface for a wavelength of either 4 μm (center of the 3-5 μm waveband) or 10 μm (center of the 8-12 μm waveband). The model choices are the Navy Aerosol Model (NAM)[6], the Open Ocean[7] model, or the TNO MPN[8] model. The vertical variation is computed after de Leeuw[9] using LKB[10] for estimating the characteristic MBL parameters and assuming that the vertical distribution for all particle sizes follows that of the 1 micron particles. The NAM model, which scales with the visibility, was used throughout this study. Calculation of the vertical refractivity profile is carried out using DREV's LWWKD[11] model for both the mid IR and far IR bands. It is an MBL model that is based upon the similarity theory work of Monin and Obukhov[12]. The results of these calculations are then passed to a DREV developed ray-tracing program[1] that is capable of calculating the change in the intensity along any ray (the refractance) using a technique developed by Blanchard[13], and calculates the molecular transmittance and aerosol transmittance by performing the integral in Eq. 3 over each ray.

3. EXPERIMENTAL DETAILS

Figure 2 shows a map of San Diego Bay that indicates the sites where the various equipment was used during the two IOPs. The Naval Postgraduate School in Monterey had positioned a "MEAN" weather buoy at the midpoint of the 7 km transmission path (between the Subbase and Coronado), and a "FLUX" weather buoy at the midpoint of the 15 km transmission path (between the Subbase and the pier at Imperial Beach). Both buoys made continuous measurements of the air temperature, water temperature, relative humidity, atmospheric pressure, wind speed and direction during most of the IOP. The FLUX buoy also made measurements of the wave spectra and their amplitudes. TNO had meteorological stations placed at both ends of the 15 km path where they measured the relative humidity, air temperature, atmospheric pressure, wind speed and direction. SPAWAR also had a meteorological station placed at the Subbase where they measured the air temperature, relative humidity, wind speed and direction, irradiance, condensation nuclei (CN), and radon. The visibility was also measured continuously at the Subbase by either DREV or SPAWAR. The air temperature, water temperature and relative humidity were also obtained, almost once a day, over the transmission path by a small boat operated by SPAWAR. SPAWAR also measured the aerosol size distribution from the boat and used Mie theory to calculate aerosol extinction coefficients at 3.5 μm and 10.6 μm.

To properly compare the waveband transmission measurements with the spectrally dependent (every $\Delta\nu = 5$ cm^{-1}) predictions from IRBLEM, the predictions must be weighted using a weighting function, w(ν), over the appropriate waveband. Following Refs. 2 & 3, the frequency dependent weighting function, w(ν), can be expressed as a function of the emission, $I_0(\nu,T)$, of the transmissometer's source, the temperature of the source, T, and the response, ε, of its detector by:

$$w(\nu) = \frac{I_0(\nu,T)\,\varepsilon(\nu)}{\int_{\nu_{min}}^{\nu_{max}} I_0(\nu,T)\,\varepsilon(\nu)\,d\nu}; \quad w_i = \frac{I_{0i}(T)\,\varepsilon_i}{\sum_{i=0}^{n} I_{0i}(T)\,\varepsilon_i \Delta\nu}. \tag{4}$$

For the TNO transmissometer[14,15,16], a dual band system which could be operated alternately in either the mid-infrared (MIR) or the far-infrared (FIR) wavelength bands and whose source has a blackbody temperature of 900 K, Fig. 3 shows the calculated weights (wΔν) of the system for both measurement periods. The difference in the two mid-infrared (MIR) responses is due to the use of different filters.

Using Eq. 4, the total waveband transmittance, $T(\nu_{min},\nu_{max})$, between the frequencies ν_{min} and ν_{max},, can be expressed by;

$$\begin{aligned} T(\nu_{min},\nu_{max}) &= \int_{\nu_{min}}^{\nu_{max}} w(\nu)\,T(\nu)\,d\nu \approx \sum_{j=1}^{m}\sum_{i=0}^{n} w(\nu_i)\,\Delta\nu\,\tau_{jM}(\nu_i)\,\rho_j(\nu_i)\,\tau_{jA}(\nu_i) \\ &\approx \sum_{j=1}^{m} \rho_j(\nu_b)\,\tau_{jA}(\nu_b) \sum_{i=0}^{n} w(\nu_i)\,\Delta\nu\,\tau_{jM}(\nu_i) \approx [\sum_{j=1}^{m} \rho_j(\nu_b)]\,\tau_A(\nu_b)\,T_M \approx \rho(\nu_b)\,\tau_A(\nu_b)\,T_M, \end{aligned} \tag{5}$$

where

$$T_M = \sum_{i=0}^{n} w(\nu_i)\Delta\nu\tau_{jM}(\nu_i), \tag{6}$$

is the waveband molecular transmittance, T(ν) is the total transmittance given by Eq. 2, and ρ (ν_b) and $\tau_A(\nu_b)$ are the refractance and aerosol transmittance for the waveband as produced by IRBLEM. Furthermore, we have assumed that the refractance and the aerosol transmittance are wavelength independent over the band, and that the molecular and aerosol transmittance are path independent. Note that the vector position, **r**, has been suppressed for clarity. From Eq. 5 we also define a normalized transmittance, $N(\nu_{min},\nu_{max})$, to be the total transmittance divided by the waveband molecular transmittance, T_M:

$$N(\nu_{min},\nu_{max}) = T(\nu_{min},\nu_{max})/T_M \ . \tag{7}$$

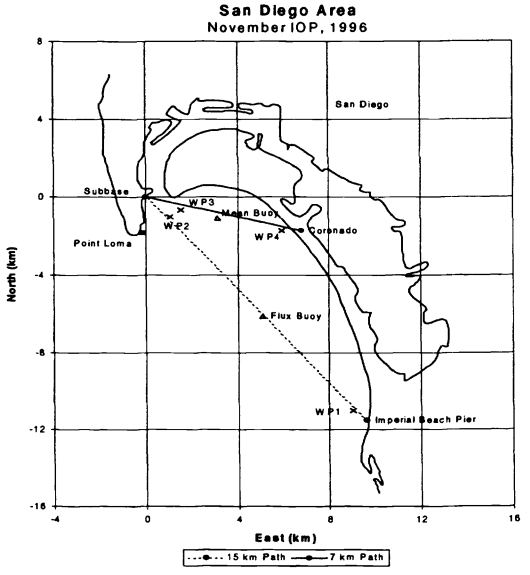

Figure 2 - Schematic map of San Diego Bay showing the placement of the two transmission paths, the two met buoys and the various waypoints.

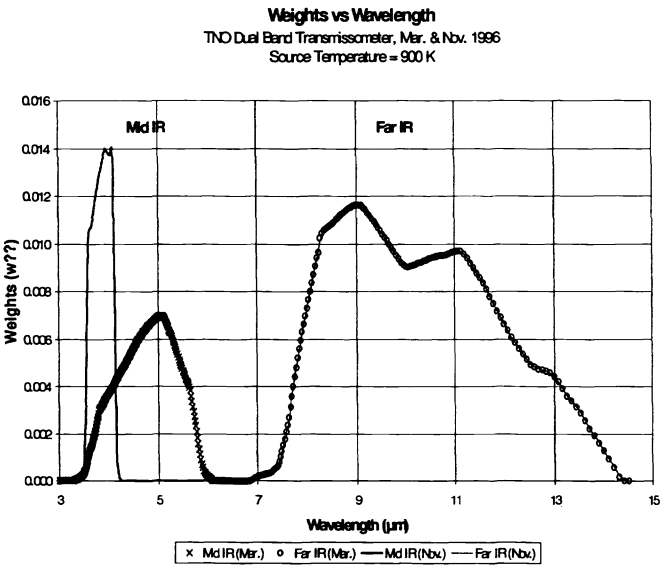

Figure 3 - Calculated weights for TNO's transmissometer for both wavebands and for both measurement periods.

4. METEOROLOGICAL MEASUREMENTS

The first six graphs (Figs. 4a,b,c and 5a,b,c) show the atmospheric conditions that prevailed during the 165 cases studied over the two week period of the first campaign in Mar.-Apr. of 1996, and the 174 cases studied over the two week period of the second campaign in Nov. of 1996. The time between subsequent cases was approximately two hours.

Figures 4a and 5a show the wind speed and direction as measured by the flux buoy over both time periods (all times in Pacific Standard Time). They show that, in general, it had a diurnal behaviour where the wind would come at low wind speeds (< 2 m/s) from a northerly to easterly (land) direction in the early morning, rise through the morning and into the afternoon to wind speeds often greater than 4 m/s and veer to come from the northwest. In the evening the winds would die down and the cycle would repeat the following morning. Exceptions to this patterns occurred on Mar. 28th, and from Nov. 14th to 16th.

Figures 4b and 5b show the variation in the virtual potential temperature for the air temperature, water temperature, and their difference as determined from measurements taken by the flux buoy. Again, an essentially diurnal pattern is prevalent with both the air and water temperatures being cooler in the early morning, warming up during the day, and then cooling down again in the evening. During both trials the water temperature was generally between 16 and 18 ^{0}C, except during the last couple of days

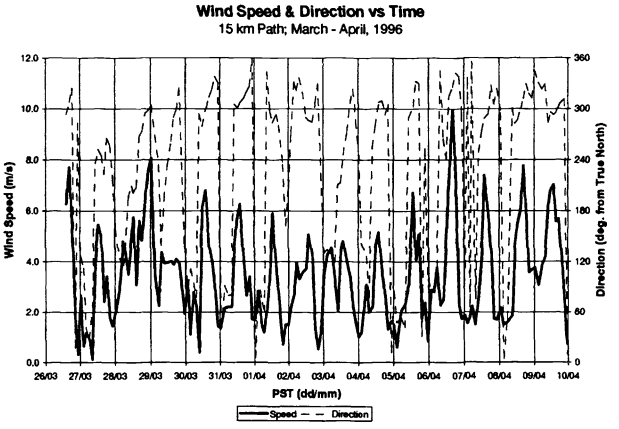

Figure 4a - Wind speed and direction as measured by the flux buoy during the March-April 1996 measurement period.

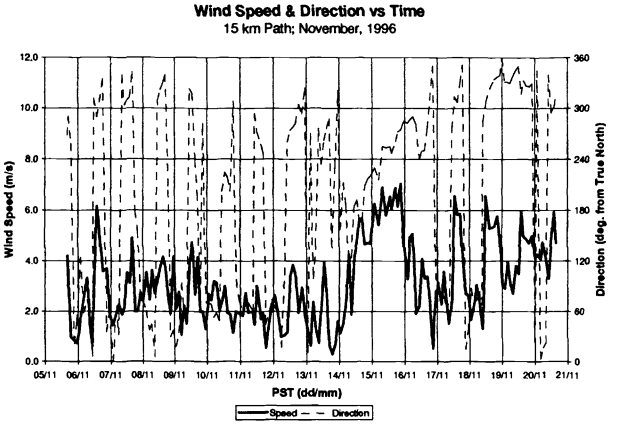

Figure 5a - Wind speed and direction as measured by the flux buoy during the November 1996 measurement period.

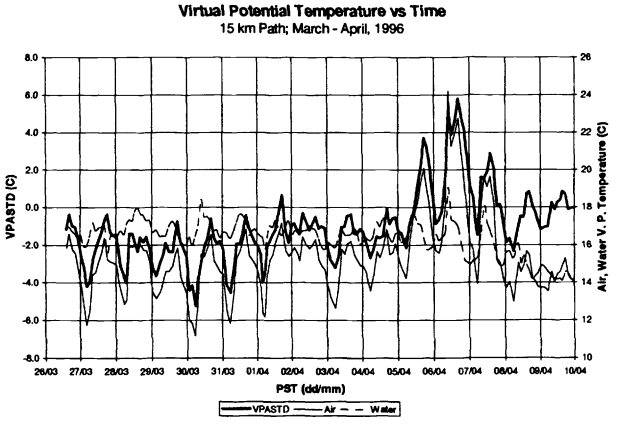

Figure 4b - Virtual potential temperatures determined from flux buoy measurements taken during the Mar.-Apr. trial (VPASTD is the virt. pot. air-sea temperature difference).

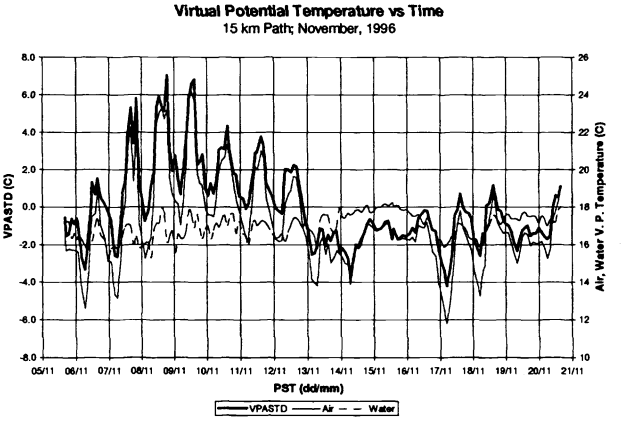

Figure 5b - Virtual potential temperatures determined from flux buoy measurements taken during the Nov. trial (VPASTD is the virtual potential air-sea temperature difference).

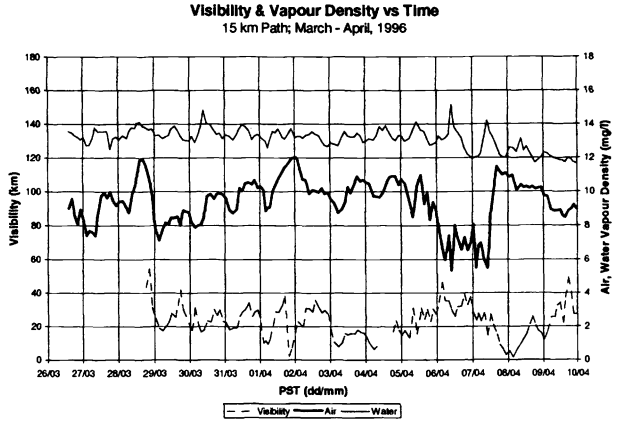

Figure 4c - Visibility measured at the subbase and the vapour density determined from measurements at the flux buoy during the Mar.-Apr. trial.

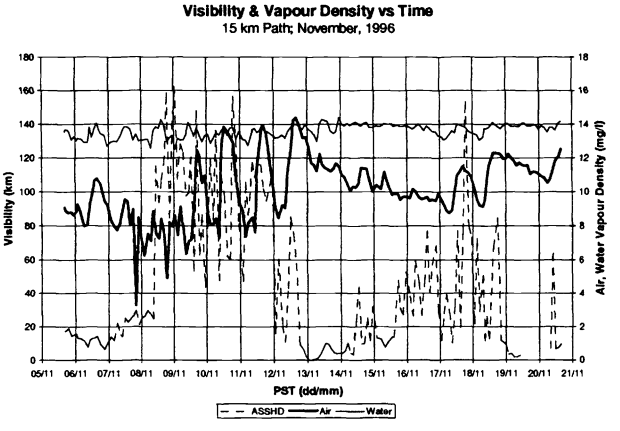

Figure 5c - Visibility measured at the subbase and the vapour density determined from measurements at the flux buoy during the Nov. trial.

during the Mar.-Apr. trial. Meanwhile, the air temperature varied from 12 to 24 ^{0}C, with daily variations often exceeding 4 ^{0}C. Two warm periods with increased daily variation were also observed. One occurred from Apr. 5th to Apr. 7th, and the other lasted almost a week from Nov. 7th to Nov. 12th. As a result, the virtual potential air-sea temperature difference (VPASTD) varied from a low of -5 ^{0}C to a high of +7 ^{0}C during the trials.

Figures 4c and 5c show the vapour density determined from measurements taken by the flux buoy and visibility measurements obtained at the subbase. As can be seen, the vapour density at the water surface is between 12 and 14 mg/liter during both trials, while the vapour density of the air probably averages 9 mg/l with variations from 5 to 14 mg/l. The reaction of the air's vapour density during the two warm periods is also interesting. One notices that at the beginning of each event the vapour density decreases for the first day or so (the air is dried out) before it rebounds to a higher level (vapour added) before falling gradually at the end of the event. In the case of the warm period in November., the vapour density also exhibits a very strong diurnal pattern after the first day or so and may indicate the occurrence of a mist or fog every night and having it burn off each morning. At the same time, the visibility varies from a couple of kilometers to over 100 km, with low visibilities occurring predominantly in the early morning and greater visibilities in the afternoon. One also notices that while the visibility tends to be inversely related to the air's vapour density, this is not always the case (particularly in the morning) and indicates that different atmospheric conditions may exist between the subbase and the flux buoy, and that one shouldn't necessarily expect the transmission path to be homogeneous.

5. ANALYSIS

Figure 6 shows the variation of the molecular transmittance calculated by IRBLEM for the three different wavebands, as seen by the detectors used during the two trials, versus the measured vapour density of the air. Second order polynomial fits to each data set are also shown. As expected, the results for the FIR waveband (x's & o's) are essentially identical for both trials and show that the FIR molecular transmittance can vary an order of magnitude. The other two curves show that the MIR waveband is less dependent on variations in the vapour density, and that the transmittance is about a factor of four greater for the narrow filter used during the November. trial than for the wider filter used during the Mar.-Apr. trial. Consequently, uncertainties in the measured vapour density will have a greater impact on the IRBLEM calculated molecular transmittances in the FIR than in the MIR.

Figures 7a,b show the results obtained for the MIR and FIR aerosol transmittances, respectively. The graphs are plotted versus the logarithm (base 10) of 1/Visibility. Thus 0.0 implies a visibility of 1 km, -1.0 a visibility of 10 km, and -2.0 a visibility of 100 km. On each graph the IRBLEM results for both trials are shown for VPASTDs less than -0.5 ^{0}C (◊'s & ○'s), and for VPASTDs greater than -0.5 ^{0}C (x's & +'s). The datasets have been divided at a VPASTD of -0.5 ^{0}C as this is the temperature difference required to negate the super-refractive effects of the pressure gradient and to create an essentially neutral boundary layer. Hence, from now on, all conditions (cases) for which the VPASTD is less than -0.5 ^{0}C will be referred to as sub-refractive conditions and all conditions for which it is greater than 0.5 ^{0}C will be referred to as super-refractive cases. The transmittance calculated using the aerosol extinction coefficients obtained from SPAWAR's aerosol measurements are shown in black (▲'s, ◆'s & ■'s). The triangles designate measurements made between 0500 and 0730 hours (PST), the diamonds for measurements made between 0730 and 1000 hours, and the squares for all other times. Finally, a sort of upper bound or fit (Heaviside Step Function) to the IRBLEM calculations under sub-refractive conditions are also given. In fact many of IRBLEM's sub-refractive predictions are within 0.1 of the fit for the FIR waveband, and within 0.2 of the fit for the MIR waveband. However, for both wave-

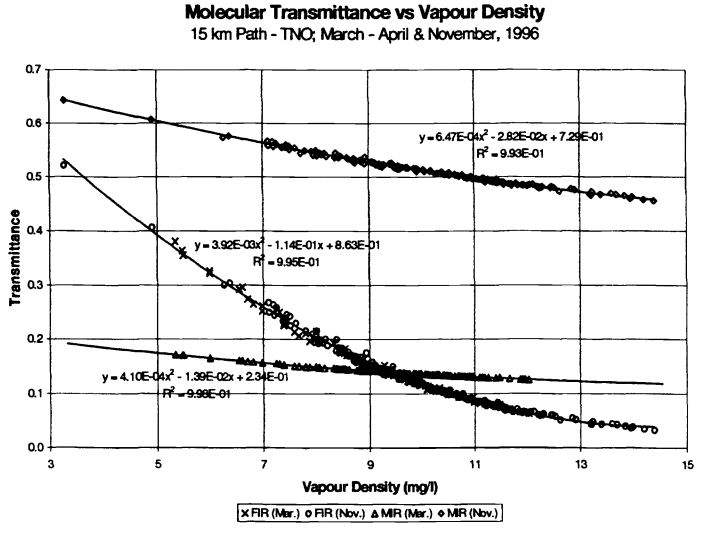

Figure 6 - IRBLEM calculated molecular transmittances for the far-infrared and the mid-infrared for both trials. The solid lines give the best 2nd order polynomial fits to the data.

bands, many of its super-refractive predictions differ significantly from the fit. This is a strange result as super-refractive conditions tend to be most prevalent in the afternoon when the air temperature is at its maximum and visibility is generally quite good. Looking at the measured aerosol data, one notes that the three lowest measurements on each graph (▲'s)were taken early in the morning on Nov. 11th and Nov. 18th and probably coincide with measurements taken in an early morning fog. The ◆'s were also taken in the morning and some of them are also well away from the fit. In most of these cases, the reason for the data not being closer to the fit is probably due to different environmental conditions (inhomogeneities along the path) being present at the flux buoy where the aerosol measurements were made, and at the subbase where the visibility measurements were taken. The fit on each graph is given by the following Heaviside step function;

$$T_A = A_1[1 + \tanh(A_2 \log_{10}(A_3 V))] = \frac{2A_1(A_3V)^{2.30A_2}}{(A_3V)^{2.30A_2} + (A_3V)^{-2.30A_2}}, \quad (8)$$

where A_1, A_2, and A_3 are (0.47, 1.7, 1.11) and (0.475, 1.7, 2.0) for the MIR and FIR bands, respectively.

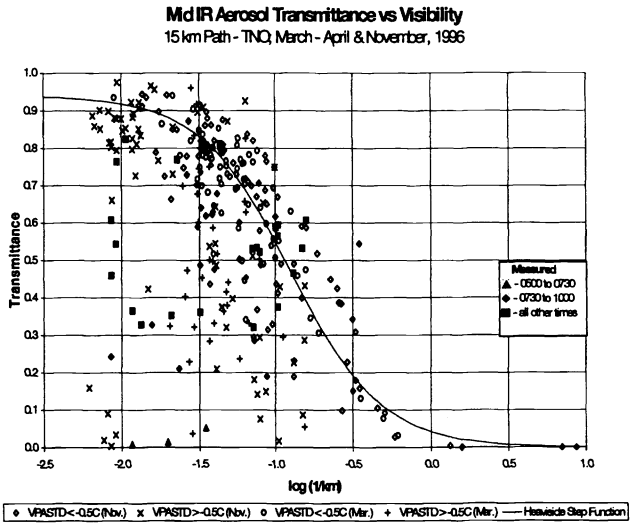

Figure 7a - MIR aerosol transmittances versus the base 10 logarithm of 1/Visibility.

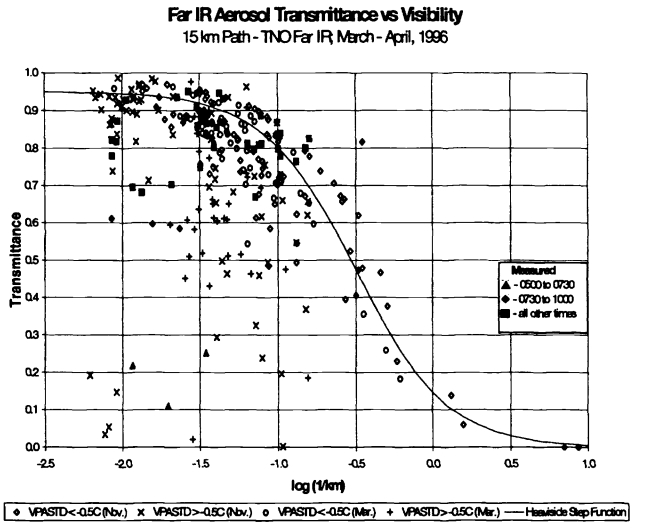

Figure 7b - FIR aerosol transmittances versus the base 10 logarithm of 1/Visibility.

Figures 8a,b show the variation of the IRBLEM calculated refractances versus the VPASTD for the MIR waveband, and versus the cut-off height (= Tide height + $H_{1/3}$ wave height above the mean water level) for the FIR waveband during the Mar.-Apr. trial. Figures 9a,b show the variation of the IRBLEM calculated refractances versus the VPASTD for the FIR waveband, and versus the cut-off height for the MIR waveband during the Nov. trial. The other four possible plots are not shown as the results are fairly similar. From Figs. 8a and 9a one notices that for the super-refractive cases (O's), the refractance generally decreases as the VPASTD increases. For the sub-refractive cases, the refractances for both the primary image (□'s) and secondary image (X's) increase with decreasing VPASTD, the refractance for the secondary image is less than that for the primary image, and both refractances easily vary by a factor of 2. The X's, at the bottom of the graphs, show cases under sub-refractive conditions when no secondary image is predicted. The ●'s correspond to sub-refractive cases when the calculated refractance is zero, in other words, the source is predicted to be below the receiver's horizon. Both graphs show that this could begin to happen when the VPASTD is below -2 °C. Furthermore, they show that during the Mar.-Apr. trial, the source is always expected to be below the horizon when the VPASTD is below -4.5 °C, and when it is below -3.5 °C during the Nov. trial. One of the reasons for the large variation in the refractance under sub-refractive conditions is due to the constantly changing geometry. While the source and the receiver are kept at constant heights above the mean water level (MWL) during the trials (the headers of Figs. 8a & 9a show these heights for both trials), their heights above the cut-off height changed continuously due to the approximately 2 m tide in San Diego, and the varying wave heights. Figures 8b and 9b show the variation of the total refractance (primary + secondary) versus the cut-off height during both trials for different VPASTD bins (each bin covers 0.5 °C). The first point to be noticed in both cases is that, apart from the super-refractive case, all the sub-refractive cases show that the total refractance increases with increasing cut-off height for each VPASTD bin. This is quite expected as the height above the actual water level, for both the

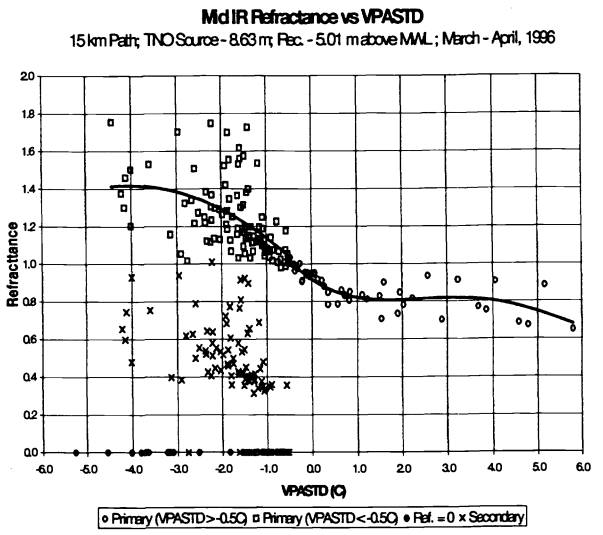

Figure 8a - Mid IR IRBLEM calculated refractances versus the VPASTD.

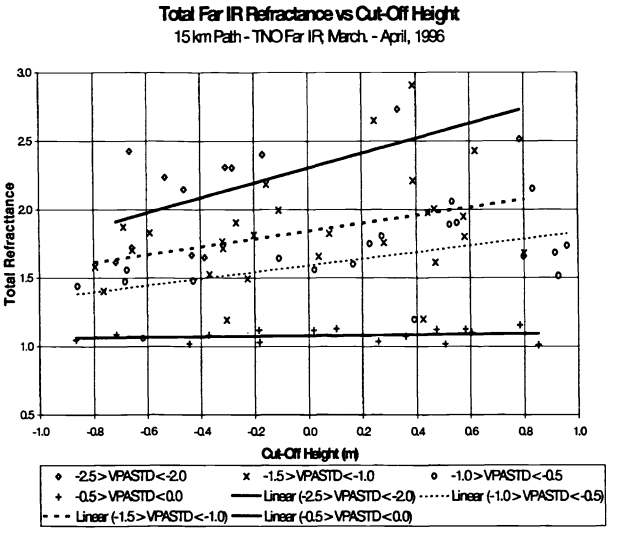

Figure 8b - Far IR IRBLEM calculated total refractances versus the cut-off height for different VPASTD bins.

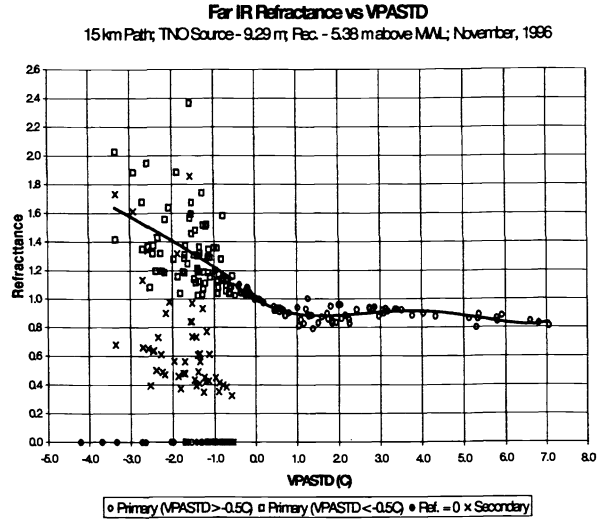

Figure 9a - Far IR IRBLEM calculated refractances versus the VPASTD.

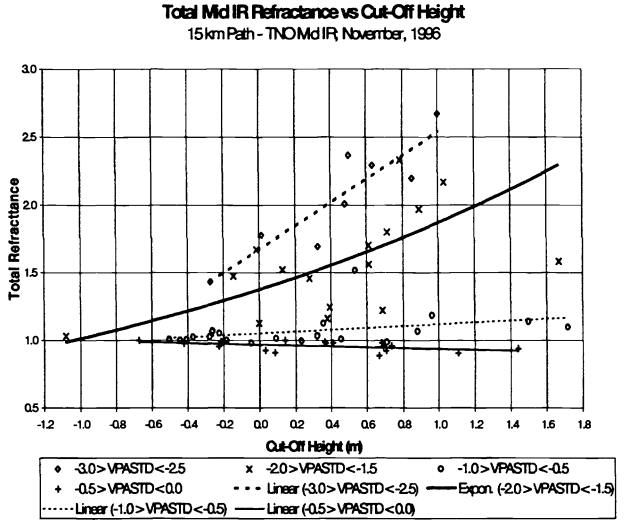

Figure 9b - Mid IR IRBLEM calculated total refractances versus the cut-off height for different VPASTD bins.

source and the receiver, decreases with increasing cut-off height and causes increased refraction effects. Likewise, when the cut-off height decreases, the source and the receiver are higher above the water level and the effects of refraction are reduced. Lastly, the rate of increase of the total refractance depends upon the VPASTD. The greater the VPASTD the faster the total refractance increases with increasing cut-off height.

Figures 10a-d show three normalized transmissions. The first is calculated using TNO's total transmittance measurements divided by the appropriate waveband molecular transmittances (T_M) calculated with IRBLEM (gray squares), the second is calculated by multiplying the refractance calculated with IRBLEM with the aerosol transmittance provided by the model fit of Eq. 8 (x's), and the third uses the aerosol transmittance provided by the model fit alone (o's; refractance assumed equal to one). Consequently, in each graph, a normalized transmission of 1.0 implies that the total transmission is equal to the appropriate IRBLEM calculated waveband molecular transmittance. Upon examination of the graphs for the Mar.-Apr. trial, one notices that, for both wavebands, the results obtained from the measured transmissions are generally less than the predictions of the model

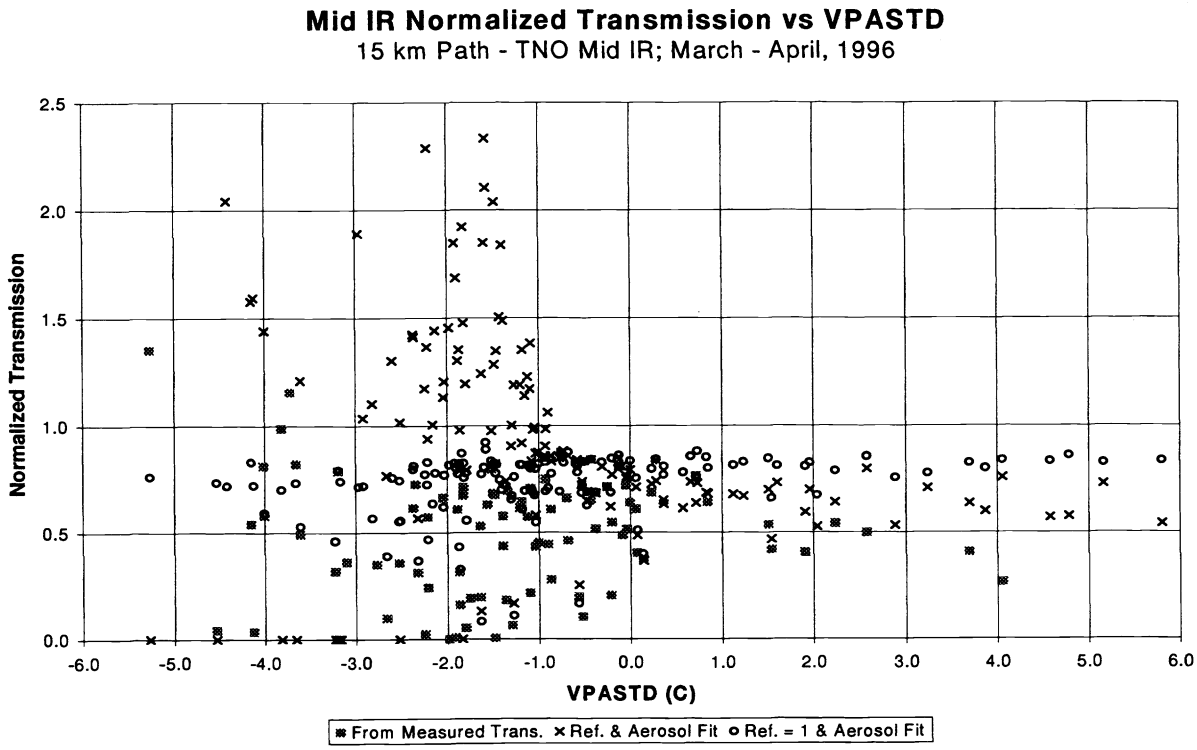

Figure 10a - Measured and calculated mid IR normalized transmissions versus the VPASTD for the Mar.-Apr. trial.

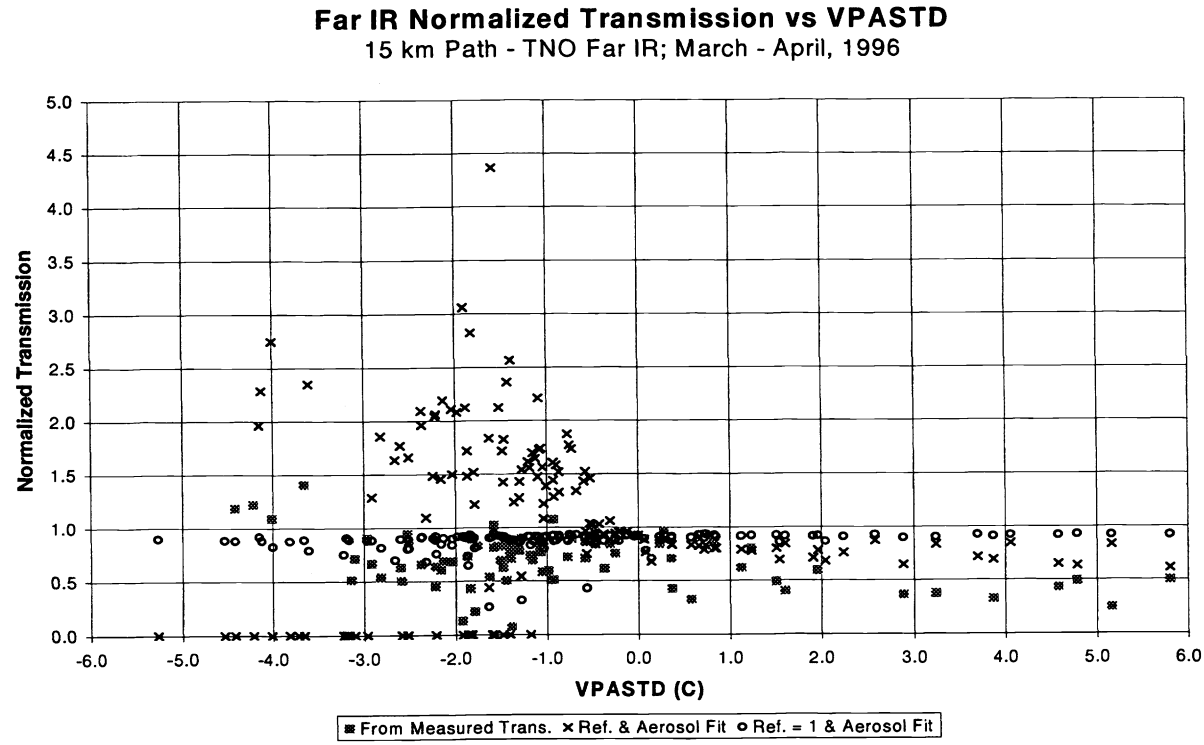

Figure 10b - Measured and calcualted far IR normalized transmissions versus the VPASTD for the Mar.-Apr. trial.

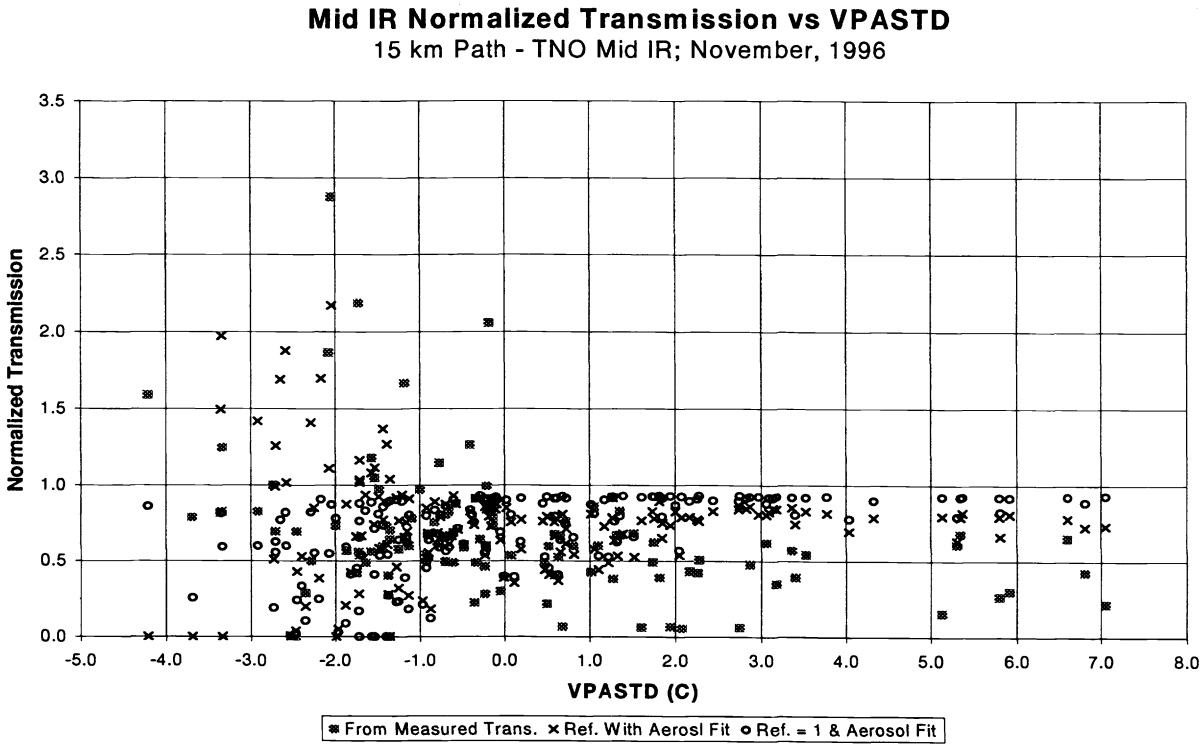

Figure 10c - Measured and calculated mid IR normalized transmissions versus the VPASTD for the Nov. trial.

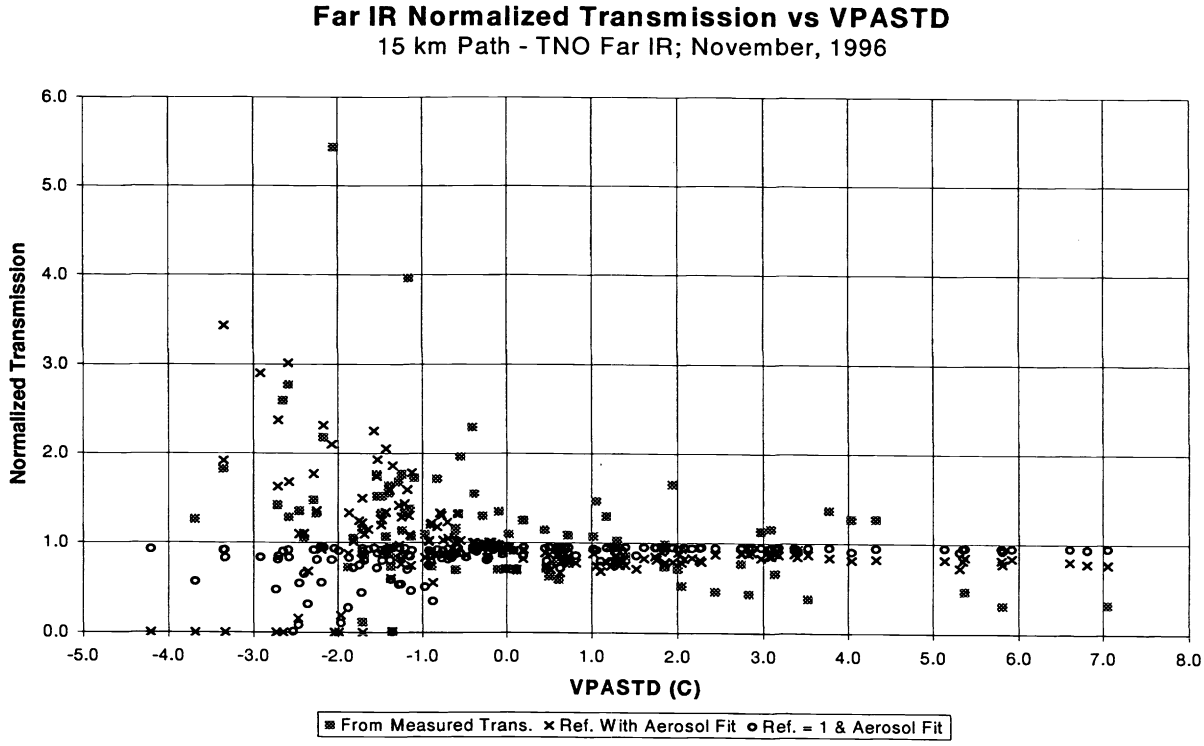

Figure 10d - Measured and calculated far IR normalized transmissions versus the VPASTD for the Nov. trial.

with refraction included, and often significantly different, as much as a factor of 2, for the sub-refractive cases. If one assumes that, under sub-refractive conditions, the refraction calculations are reasonably correct, one is left with the possibility that either the aerosol transmittance must be substantially less than indicated (a factor of 2) for many of the sub-refractive conditions, or that the calculated waveband molecular transmittances are somewhat greater (say 1.5 times) than expected. If one assumes that the aerosol and molecular calculations are correct, then one is left with a problem with the refractance calculation and possibly with the models determination of the refractive index's vertical gradient. Looking at the graphs for the November trial, one notices that, for both wavebands, the results obtained from the measured transmissions under sub-refractive conditions more closely resemble the range of the model predictions with refraction included. However, under super-refractive conditions, while the measured transmissions for the MIR are often significantly less than the model predictions with refraction, the measured transmissions for the FIR tend to jump around the model's predictions and are occasionally greater than 1. This is a bit troublesome, as this tends to indicate that the calculated waveband molecular transmissions may not be as great as they should be. The problem is that this contradicts one of the possible reasons for the disagreements seen in the Mar.-Apr. data, and leaves us with reasons related to possible inhomogeneities along the transmission path.

6. CONCLUSIONS

IRBLEM calculations from over 300 meteorological conditions over two different IOP's of the EOPACE trial have been compared with actual transmission measurements for both the mid infrared and far infrared wavebands. The results of our study show that the IRBLEM calculated waveband molecular transmittances for a fixed geometry can be very well modelled as a function of water vapour density. It also shows that the FIR waveband is much more sensitive to changes in water vapour density than the MIR band, and that the bandwidth of the detector can have a significant affect on the predicted molecular transmittance. Thus, good quality measurements of the water vapour density and the response of the detector are absolutely essential if one is to obtain reliable results from IRBLEM's calculation of the waveband molecular transmittance.

From IRBLEM's aerosol transmittance calculations we noticed that there was, not unexpectedly, a certain relationship with the visibility, and that this relationship is more clearly defined in the FIR than in the MIR. A number of the measured aerosol transmittances also pointed out possible problems due to inhomogeneities along the transmission path and the need, though difficult, to make high quality visibility measurements at the flux buoy.

IRBLEM's refractance calculations show that under super-refractive conditions (VPASTD > -0.5 °C), the refactance tends to decrease, from a value near unity to values between 0.7 and 0.8, with increasing VPASTD. The refractance is also relatively independent of changes in geometry due to the tide and wave heights. However, under sub-refractive (VPASTD < -0.5 °C) conditions, the refractance is highly dependent on these same changes in geometry. As shown, for a particular VPASTD, the refractance increases with increasing cut-off height (tide height + wave height above the MWL) until it drops to zero (source below the horizon). Furthermore, the more negative the VPASTD, the faster the refractance increases and the sooner it drops to zero. As a result, it is very important to make good reliable measurements of the air and sea surfaces' virtual potential temperatures near the middle of the transmission path, and to have good measurements of the source height, receiver height, variations in the tide, and changes in the height of the waves.

The possible problems involved in calculating the waveband molecular transmittance, the aerosol transmittance, and the refractance are all evident when comparing the results from the measured transmissions with the calculations. In order to resolve the reasons for these differences a partitioning of the data along several lines is required. First, as was done in this study, the data should be partitioned between sub-refractive and super-refractive cases. This allows us to divide the cases between those which have and those which don't have a strong dependence upon the experimental geometry. Secondly, cases where conditions along the transmission path are not expected to be relatively homogeneous should be removed. This is not an easy task, and will probably require looking more closely at the videotape records which were made during the two trials, and at the other measurements taken around the bay, to see how well the visibility measurements at the subbase concur with the other observations and how well the measurements taken at the different locations are in agreement.

Finally, while predictions made using the IRBLEM model can often agree with the TNO measurements, they can also be in strong disagreement. Many reasons can be put forth to explain these differences, from problems with the transmission data and the use of unrepresentative meteorological data in the model; however, with each look at a new or older dataset, our analysis techniques are being refined and the importance of certain meteorological measurements are being further highlighted.

ACKNOWLEDGEMENTS

Special mention must be made acknowledging the efforts of Douglas Jensen of SPAWAR, whose efforts have allowed EOPACE to come to life and develop into an excellent program.

REFERENCES

1. D. Dion and P. Schwering, "On the Analysis of Atmospheric Effects on Electro-Optical Sensors in the Marine Surface Layer", IRIS Conference, UK, June 1996.
2. J.L. Forand, M. Duffy, C. Zeisse, S. Gathman, A. de Jong, and D. Dion, "Atmospheric Effects on Low Elevation Transmission Measurements at EOPACE", Proc. SPIE, Vol. 3125, Propagation and Imaging throug the Atmosphere, pp. 123-134, 1997.
3. J.L. Forand, D.Dion, M. Duffy, A. de Jong, G. de Leeuw, S. Gathman, K. Littfin, P. Frederickson, and K. Davidson, "Low-Level IR Transmission Measurements over a 15 km Littoral Path", Proc. Of the 1997 Battlespace Atmospherics Conf., 2-4 Dec. 1997, pp. 579-588.
4. A. Beck, L. S. Bernstein, D. C. Robertson, "MODTRAN: A Moderate Resolution Model for LOWTRAN 7", Final Report, Spectral Sciences, Inc., Burlington, MA, 1989.
5. P. Schwering and G. Kunz, "Infrared scintillation effects over sea", SPIE Proc., Vol. 2471, pp. 204-215, 1995.
6. S. G. Gathman, "Optical properties of the marine aerosol as predicted by the Navy Aerosol Model", Opt. Eng., Vol. 22(1), pp. 57-62, 1983.
7. G. de Leeuw, A.M.J. van Eijk, and G. R. Noordhuis, "Modeling aerosols and extinction in the marine atmospheric boundary layer", Proc. SPIE., Vol. 1968, pp. 70-80, 1993.
8. A.M.J. van Eijk and G. de Leeuw, "Modeling aerosol particle size distributions over the North Sea", Journal of Geophysical Research, Vol. 97C, pp. 14417-14429, 1992.
9. G. de Leeuw, "Modeling of extinction and aerosol backscatter profiles in the marine mixed layer", Applied Optics, Vol. 28, pp. 1356-1359, 1989.
10. W. T. Liu, K.B. Katsaros, and J.A. Businger, "Bulk Parametrization of Air-Sea Exchanges of Heat and Water Vapor Including the Molecular Constraints at the Interface", Journal of Atmospheric Sciences, Vol. 36, pp. 1722-1735, 1979.
11. J. L. Forand, "The L(W)WKD Marine Boundary Layer Model", DREV R-9618, March, 1997, UNCLASSIFIED.
12. A. S. Monin and A. M. Obukhov, "Basic Regularity in Turbulent Mixing in the Surface Layer of the Atmosphere", Trad. Geophys. Inst. ANSSSR, No. 24, p. 163, 1954.
13. A. Blanchard, "Phase and intensity ray tracing to study the propagation of coherent radiation in the atmosphere and other media", DREV R-4699, 1993, UNCLASSIFIED.
14. C.R. Zeisse, S.G. Gathman, A.N. de Jong, G. de Leeuw, J.L. Forand, D. Dion and K.L. Davidson, "Low Elevation transmission measurements at EOPACE part 1: molecular and aerosol effects", SPIE Proc., Vol. 3125, 1997.
15. A.N. de Jong, G. de Leeuw and K.L. Davidson, "Low elevation transmission measurements at EOPACE part III: scintillation effects", SPIE Proc., Vol. 3125, 1997.
16. A.N. de Jong and P.J. Fritz, "EOPACE Transmission Experiments Spring 1996; Preliminary Results", TNO Report, FEL-96-A090, March 1997.